Full-Scale Test and Analysis Results of a PRSEUS Fuselage Panel to Assess Damage Containment Features

Andrew Bergan[1], John G. Bakuckas, Jr.[2], Andrew Lovejoy[3], Dawn Jegley[3], Kim Linton[4], Bert Neal[5], Gregory Korkosz[6], Jonathan Awerbuch[7], and Tein-Min Tan[7]

[1]FAA-Drexel Fellowship Student, FAA William J. Hughes Technical Center, Atlantic City International Airport, NJ 08405, USA

[2]FAA William J. Hughes Technical Center, Atlantic City International Airport, NJ 08405, USA

[3]NASA Langley Research Center, Hampton, VA 23681, USA

[4]Boeing Research and Technology, 2201 Seal Beach Blvd., Seal Beach, CA 90740, USA

[5]Boeing Research and Technology, 8900 Frost Ave., Bldg. 245, Berkeley, MO 63134, USA

[6]Legacy Engineering, 5954 Paseo Canyon Drive, Malibu, CA 90265, USA

[7]Department of Mechanical Engineering and Mechanics, Drexel University, Philadelphia, PA 19104, USA

I. ABSTRACT

Integrally stitched composite technology is an area that shows promise in enhancing the structural integrity of aircraft and aerospace structures. The most recent generation of this technology is the Pultruded Rod Stitched Efficient Unitized Structure (PRSEUS) concept. The goal of the PRSEUS concept relevant to this test is to provide damage containment capability for composite structures while reducing overall structural weight. The National Aeronautics and Space Administration (NASA), the Federal Aviation Administration (FAA), and The Boeing Company have partnered in an effort to assess the damage containment features of a full-scale curved PRSEUS panel using the FAA Full-Scale Aircraft Structural Test Evaluation and Research (FASTER) facility. A single PRSEUS test panel was subjected to axial tension, internal pressure, and combined axial tension and internal pressure loads. The test results showed excellent performance of the PRSEUS concept. No growth of Barely Visible Impact Damage (BVID) was observed after ultimate loads were applied. With a two-bay notch severing the central stringer, damage was contained within the two-bay region well above the required limit load conditions. Catastrophic failure was well above the ultimate load level. Information describing the test panel and procedure has been previously presented, so this paper focuses on the experimental procedure, test results, nondestructive inspection results, and preliminary test and analysis correlation.

II. INTRODUCTION

Integrally stitched composite technology shows promise in enhancing the structural integrity of aircraft and aerospace structures. NASA, Boeing, and the FAA have partnered to assess the damage containment features of the most recent generation of stitched composite technology, the PRSEUS concept [1-5]. Tests have been conducted on flat-element and full-scale PRSEUS specimens; however, no tests of curved PRSEUS structures have been completed prior to this

study. In addition, prior tests have applied either unidirectional loading or pressure only. The current study includes, not only internal pressure and axial tension applied separately, but also combined loading, including both axial tension and internal pressure. The purpose of this joint design, build, and test program was to show that a curved PRSEUS panel meets the strength, deformation, and damage tolerance requirements described in Title 14 Code of Federal Regulations (CFR) Part 25 [6] and to characterize the damage containment features of a curved PRSEUS panel. To accomplish these goals, a curved PRSEUS panel was fabricated by Boeing and loaded in a series of tests at the FAA FASTER facility. The FASTER fixture was modified to enhance the axial loading capacity [7] to accomodate the higher load capacity of the PRSEUS panel. The purpose of this paper is to provide an overview of the experimental procedure, test results, and preliminary test and analysis correlation of the curved PRSEUS panel.

The test program included three phases of loading and inspections: Phase I—as-built, which provided a baseline for comparison between test and analysis of an undamaged panel; Phase II—with BVID, which documented damage growth typical of undetected damage in operation environment; and Phase III—with a two-bay notch severing the central stiffener, which demonstrated the robustness of the design and the ability to support loading, even with severe damage. Axial tension, internal pressure, and combined axial tension and internal pressure load conditions were applied during each phase using load levels that demonstrate compliance with the strength, deformation, and damage tolerance requirements of 14 CFR Part 25. Pressure loads were based on an operating pressure of 9.2 psi, designated as 1P, and the axial loads were based on a design limit load (DLL) of 227 kip total. The criteria for evaluating the performace of the panel were sustaining (1) limit loads with no permanent damage and no growth of BVID, (2) ultimate loads without failure, and (3) limit loads with a two-bay notch. These criteria are based on Boeing engineering practice, guidance from FAA Advisory Circulars (AC) 20-107B [8] and 25.571-1D [9], and satisfying the requirements of 14 CFR Part 25 for strength and deformation (§305), and damage tolerance (§571).

In this paper, the experimental procedure is described first, including a brief overview of the test panel configuration, test phases, load history, and inspection and monitoring methods. Next, the analytical procedure is reviewed. Finally, results are presented for each test phase.

III. EXPERIMENTAL PROCEDURE

3.1 Test Panel Configuration

The fuselage panel's overall size was 127-inch long and 75-inch wide, with a 90-inch radius. It contained seven full-length rod-stiffened stringers and five foam core frames, as shown in Figure 1. The panel was intended to represent a section of an aircraft fuselage, comprising the portion of the panel enclosed by the second and fourth frames and outermost stringers, as shown highlighted in blue and labeled "test section" in Figure 1(a). The remainder of the panel incorporates thickness pad-ups to provide transition of the test section to the load introduction structure. The carbon epoxy panel was constructed primarily from AS4 fibers with a VRM 34 resin in a vacuum-assisted resin transfer molding cure process. The stringers and frames were integrally stitched to the skin using a single-sided stitching process with Vectran® thread shown by the red-dashed arrows in Figure 1(b) and (c). Several plies were co-cured around the perimeter of the panel and at the frame ends for load introductions purposes. Details of the test

panel geometry, materials, lay-up, load introduction reinforcements, and fabrication process are available in references 7 and 10.

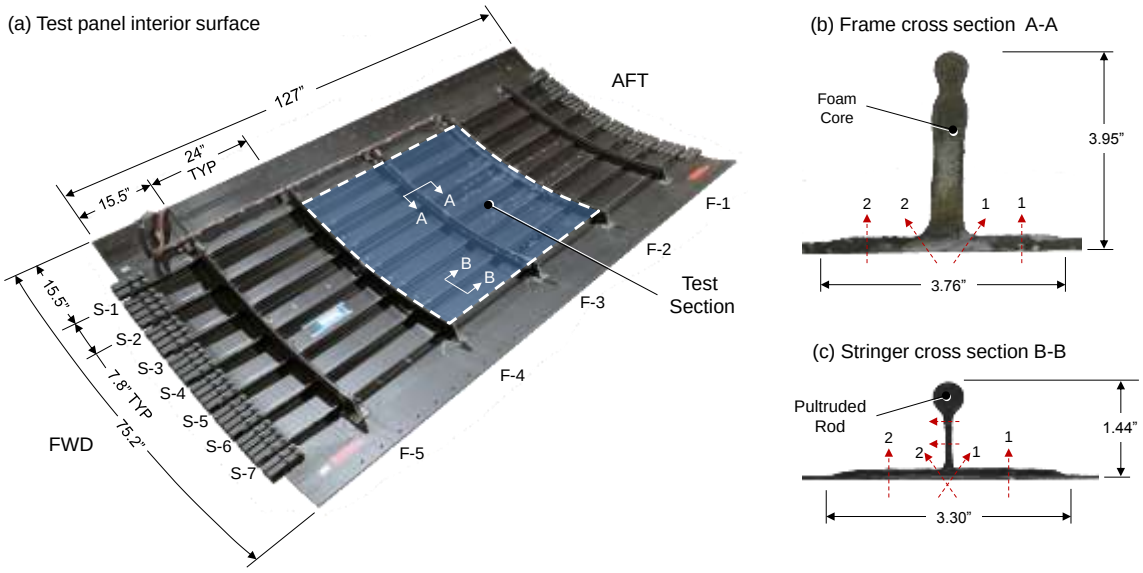

Figure 1. Photographs of the PRSEUS Test Panel Configuration

3.2 Test Phases and Load History

The modified FASTER fixture used two sets of seven axial loaders aligned with the stringers at each end of the panel, two sets of seven hoop loaders along each straight edge of the panel, and two sets of five frame loaders connected directly to the frame ends to apply load [7].

Table 1 summarizes the test phases and load history applied to the panel. Additional checkout tests were conducted and are not listed. Loading was monotonically applied for all load conditions except in Phase III, in which loads were transitioned between the load conditions that included limit pressure, combined pressure and axial load, and axial loads only. For cases in which pressure load was applied, axial, skin hoop, and frame loads were also applied to react the internal pressure to maintain equilibrium assuming a closed pressure vessel. The axial load magnitudes for combined load cases are a combination of applied axial load and the reaction load from internal pressure.

Table 1. Test Sequence

	Load Condition	Relative Applied Loads*	
		Axial(% DLL)	Pressure (% P)
Phase I	Axial	100	-
	Combined	100	100
	Pressure	-	133
Phase II	Axial	100	-
	Pressure	-	133
	Combined	100	100
	Pressure	-	200
	Axial	150	-
	Combined	150	150
Phase III	Pressure	-	115
	Combined	100	100
	Axial	100	0
	Failure	184	100

*Loads relative to limit load magnitude.

An overview of each test phase, including the load history of the final load case, is presented in the following section.

3.2.1 Phase I: Pristine Case

The purpose of Phase I tests was to show repeatability of strain and displacement results, to provide baseline results in the as-built condition for correlation with analytical models, and to demonstrate compliance with the limit strength and deformation requirement of 14 CFR 25.305. The Phase I test results provided a baseline by applying (1) 50% limit load levels for each of the three load cases and (2) three limit load conditions (limit pressure of 12.2 psi (1.33P), axial DLL of 227 kip, and combined 1P pressure and axial DLL). Half load tests were conducted to verify proper load introduction and repeatability by examining strain and displacement results. For the combined load case, pressure load was applied and stabilized, then axial load was applied to the target load; this sequence was reversed for unloading.

3.2.2 Phase II: Barely Visible Impact Damage Case

The purpose of Phase II tests was to demonstrate that the panel with BVID met the ultimate strength and deformation requirement of 14 CFR 25.305 and guidance of AC 20-107B. The damage was created using a drop weight impactor with a 25-lb weight and a 1-inch-diameter hemispherical tup impactor. The location of the BVID was over the central stringer, S-4, between frames F-2 and F-3, as shown in Figure 2. An impact, with 40-ft-lb impact energy, was applied to a location between the central-stringer flange edge and the outer stitch row, as shown in Figure 2(b) and (c). A secondary impact was prevented by positioning a paddle over the impact site immediately after the first impact, which prevented the drop weight from striking the panel multiple times.

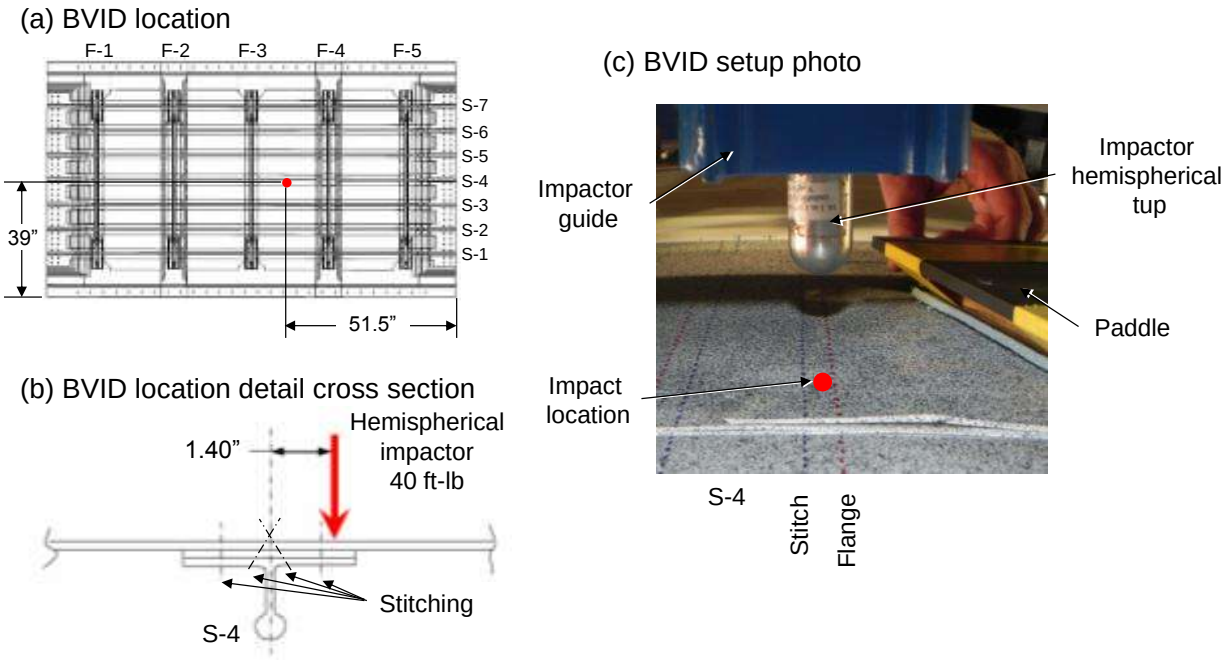

Figure 2. Phase II BVID Location and Test Setup

Photographs of the impact site are shown in Figure 3. The baseline condition is shown in Figure 3(a). After impact, visual inspection showed little indication of fiber breakage or a dent on the exterior surface, as shown in Figure 3(b), which are criteria indicating a severe BVID [7]. The panel was impacted a second time in the same location with the same impact energy, which created clearly visible fiber breaks over an area of 0.16 by 0.38 inch on the exterior surface and visible fiber breaks and delamination on the interior surface, as shown in Figure 3(c) and (d), respectively. Therefore, this damage was classified as very severe BVID that was deemed acceptable for the purpose of this test. The impact depth was 0.015 in. The impact region was inspected using visual, ultrasound, and flash thermography techniques before impact (baseline), after impact, and after each case. Three limit load conditions were applied, followed by three ultimate load conditions: (1) pressure overload of 18.4 psi (2P), (2) ultimate axial load (150% DLL), and (3) ultimate combined load conditions (1.5P + 150% DLL).

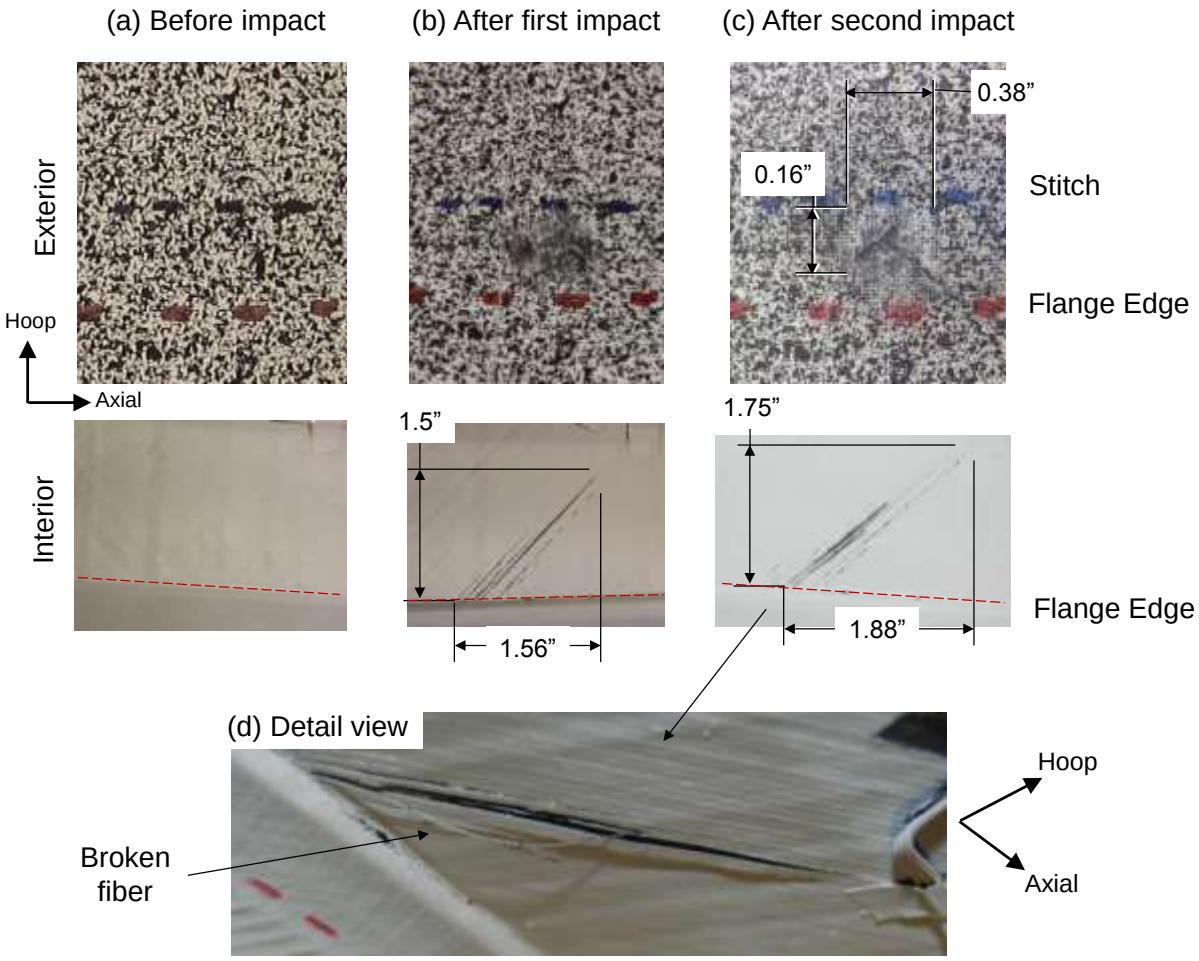

Figure 3. Photographs of the BVID, as Seen From the Exterior and Interior, Before and After Impact

3.2.3 Phase III: Two-Bay Notch Damage Case

The purpose of Phase III was to demonstrate compliance with 14 CFR 25.571 by showing that the panel could support limit loads with a two-bay notch severing the central stringer, and then to monitor the failure process while increasing the axial load until catastrophic failure occurred. The notch was machined over the BVID at the location shown in Figure 4(a) using a 5/16-inch router bit and a machining template. The impact damage site was partially removed during the notch machining to minimize the effects on Phase III results, as shown in Figure 4(b). The notch was 7.8-inch long by 0.31-inch wide and was placed symmetrically across stringer S-4, as shown in Figure 4(b). The notch was through the thickness and severed both the skin and the central stringer, as shown in Figure 4(c) and (d), respectively.

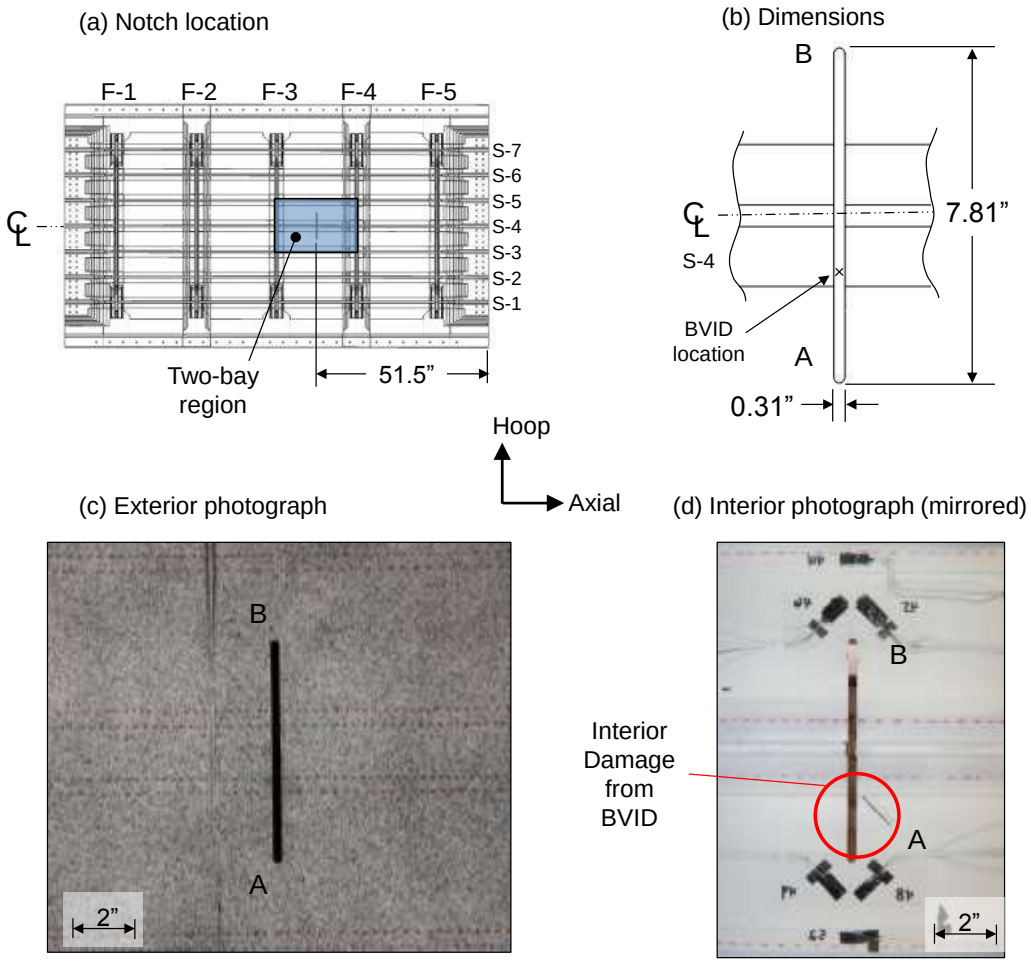

Figure 4. The Two-Bay Notch

After the notch was machined the panel was subject to limit load conditions, followed by combined 1P pressure while increasing axial tension load to catastrophic failure. The final load sequence to failure incorporated a complex load history, so all target load conditions were achieved without completely unloading the panel, which was done to eliminate concerns of additional damage formation during unloading. The load history for the final load case is shown in Figure 5, and the load step descriptions are in Table 2. The panel was subjected to three load conditions in the order of increasing severity, as predicted by the pretest analytical model [7]: pressure (1.15P), combined pressure and axial (1P + DLL), and axial (DLL) load conditions; followed by maintaining pressure (1P) and increasing axial load to catastrophic failure. During the final load step, the hydraulic pump briefly shut off resulting in a short duration of constant axial load that was followed by axial loading at a faster loading rate.

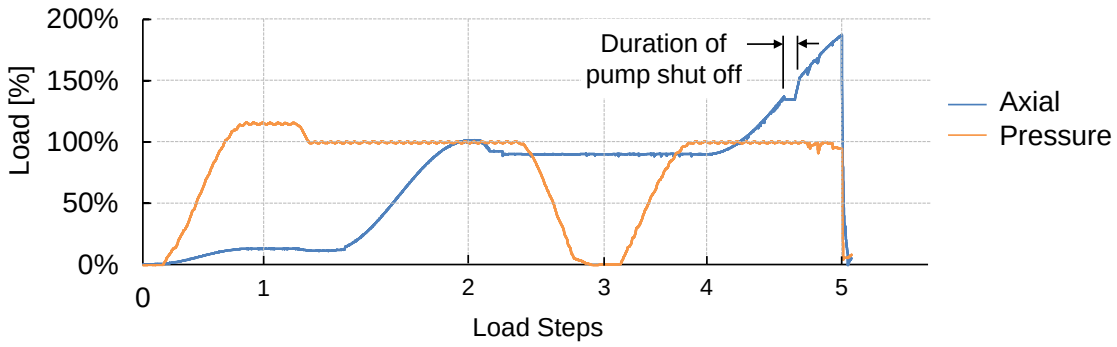

Figure 5. Final Load Case Loading History (Numbered steps are described in Table 2.)

Table 2. Phase III Load Steps

Load Step	Load Levels		Load Changes
	Axial (% DLL)	Pressure (% P)	
1	--	115	Pressure increased to 1.15P
2	100	100	Pressure reduced to 1P then axial load increased to DLL
3	100	--	Axial reaction to pressure removed, then pressure removed
4	100	100	Pressure increased to 1P
5	184	100	Axial load increased to catastrophic failure

3.3 Inspection and Monitoring Methods

Test results were acquired using visual, strain and displacement, and damage detection methods. The inspection and monitoring methods are summarized in the following sections.

3.3.1 Visual Inspection

Visual inspection tools were used for monitoring panel behavior during the test and included interior and exterior video cameras, a high-resolution exterior still camera, and two high-speed video cameras, as shown in Figure 6. The two high-speed cameras were only used during Phase III.

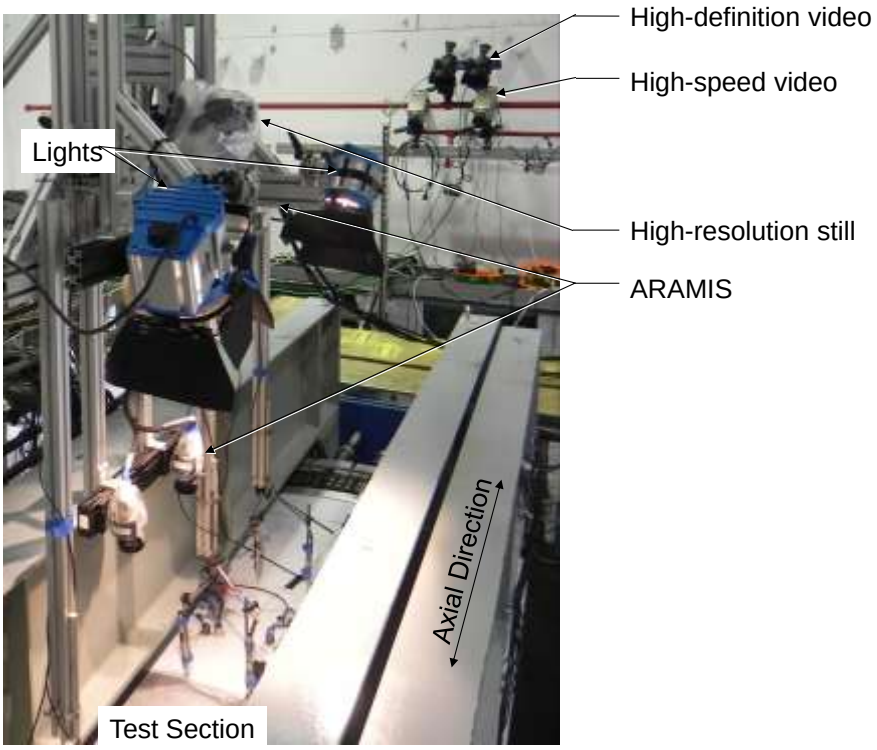

Figure 6. Photograph of the Visual Monitoring Setup

3.3.2 Strain and Displacement

Eighty strain gages, eleven linear variable displacement transducers (LVDT), and two ARAMIS™ [11] photogrammetry systems were used to record strain, displacement, and deformation data. The test panel was instrumented with strain gages in the axial, hoop, and 45° directions to monitor real-time strain distribution to ensure proper load introduction from the load application points and to monitor strains in critical regions. The strain gage locations and orientations on the exterior and interior surfaces are shown in Figures 7 and 8, respectively. Several strain gages were installed in a back-to-back configuration to monitor the bending response of the panel. Interior strain gages were coated to operate underwater because water is the pressurization medium used in the FASTER fixture. The LVDTs measured the axial and radial displacements and are shown on the exterior of the panel in Figure 7. LVDT 1 was mounted on a frame so that it measured the displacement between the two points shown; whereas, all other LVDTs measured displacements relative to ground. Measurements from LVDT 1 and 2 were used to eliminate axial rigid-body motion from the results. During the test, all strain and displacement data was recorded to a circular buffer at a rate of 10 Hz. The ARAMIS systems were positioned to monitor strains and deformation in the test section, including strain concentrations ahead of the notch tips during Phase III.

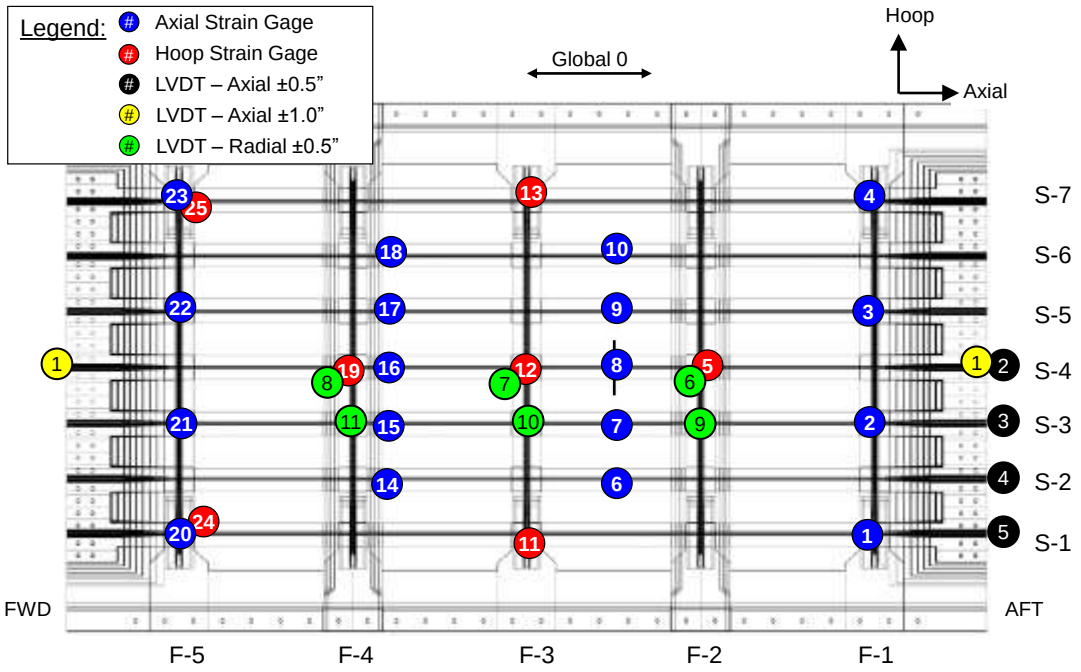

Figure 7. Exterior Strain Gage and LVDT Locations

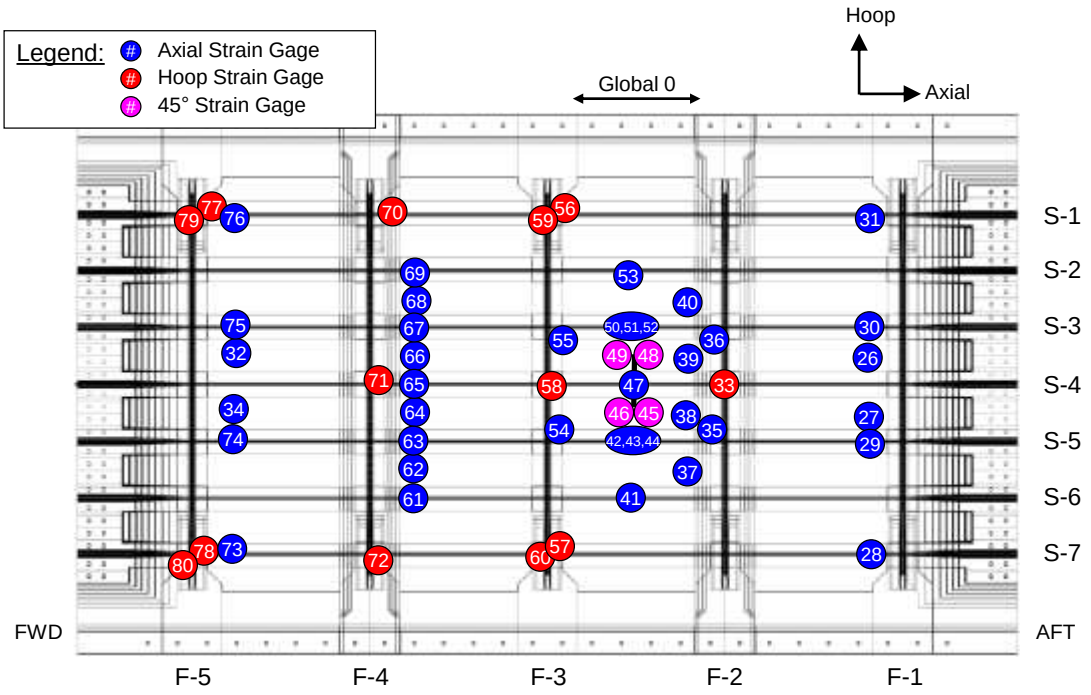

Figure 8. Interior Strain Gage Locations

3.3.3 Portable C-Scan

Pulse-echo ultrasonic scans were taken using a linear phased array at 10 MHz. The Olympus OmniScan MX2 with PA16/128 module was used in conjunction with a 10L64-I1 sensor in a

NASA-captured water column mounting. Scans were performed using a Sonix 18- by 18-in. manual scanner positioned with the index axis in the axial direction, so the scan axis was in the hoop direction of the panel. Scans were taken after the completion of Phase 1, after impact, and after each load condition in Phase II.

3.3.4 Flash Thermography

A flash thermography system was used to inspect the test section for nonvisual damage, as shown in Figure 9. The system consists of a computer that contains data acquisition hardware and software connected to a flash lamp heat source and thermal infrared camera. A brief pulse of light energy from a flash lamp was used to heat the surface of the specimen, while an infrared camera recorded changes in the surface temperature as the specimen cooled. The surface temperature, which fell predictably as heat from the surface diffused into the sample, was affected by internal flaws that obstructed the flow of heat. The system provides a 6- by 5-in. image and can be set up to take a grid of images to scan large areas. A baseline scan of the panel was taken prior to Phase I, II, and III. During Phase II, scans were taken after each load condition. After catastrophic failure, a scan was taken of the entire width of the panel between frames F-2 and F-3.

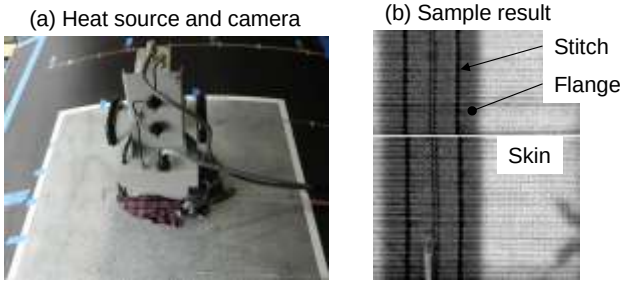

Figure 9. Flash Thermography System

IV. ANALYTICAL PROCEDURE

A linear elastic finite element model (FEM) was developed using NASTRAN with shell and bar elements representing the panel and FASTER fixture. The purpose of the model was to define the load application sequence, load levels to attain the target strain levels in the test section, required boundary conditions, and to predict failure mode and strains. The model contained the details and dimensions of the panel, including the skin, frames, stringers, and load introduction buildups, as shown by the mesh in Figure 10. Stiff bar elements were used to model the FASTER fixture loaders for an accurate representation of the boundary conditions. No damage was modeled; hence, results are only available for Phase I. The model was calibrated based on the 50% load tests and was used to predict strains and displacement in the subsequent tests. More detail on the model can be found in reference 10. Results from the model are compared to experimental results in the following section.

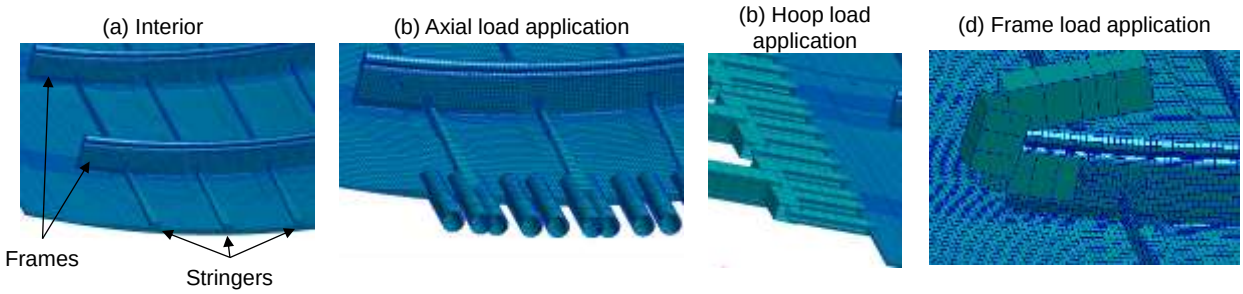

Figure 10. Typical FEM Mesh Showing the Panel Modeled as Shell Elements and FASTER Fixture Loaders Modeled as Stiff Bar Elements

V. RESULTS AND DISCUSSION

An overview of the experimental results for the three test phases is presented in the following sections.

5.1 Phase I

The Phase I test results provide a baseline for the PRSEUS curved panel response. First, 50% limit load levels were applied for each of the three load conditions to verify proper load introduction and repeatability by examining strain and displacement measurements. At least two cycles were run at the 50% limit load magnitudes for each of the three loading conditions. Strain and displacements from two combined load cycles are shown in Figure 11, which indicate excellent repeatability. Next, three limit load cases were applied: limit pressure of 1.33P, axial DLL, and combined 1P pressure and axial DLL. Strain and displacement results were recorded for all load conditions.

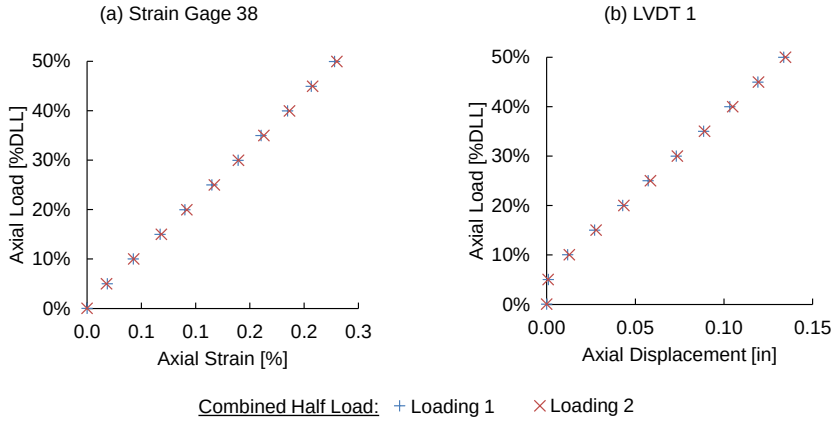

Figure 11. Typical 50% Limit Load Strain and Displacement Results for Two Combined Load Conditions

Strain and displacement results were also compared with FEM predictions at 50% and 100% limit load magnitudes for the three load conditions. In general, good agreement between experimental results and analytical predictions was observed. Representative strain and displacement results for the combined limit load (1P + 100% DLL) are shown in Figure 12.

Good agreement was observed between experimental and FEM predicted strains in the test section. The displacement results showed a consistent trend with analysis, both indicating a parabolic edge displacement profile.

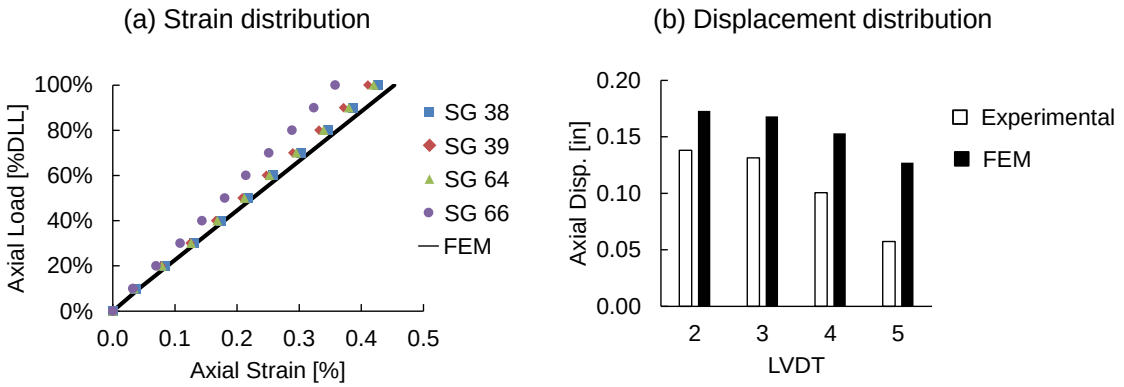

Figure 12. Limit Load Strain and Displacement Distributions for the Combined Load Condition

In general, ARAMIS results show a uniform strain distribution in the test section and demonstrate good agreement with strain gage results. A representative case is shown for combined limit load (1P + 100% DLL) in Figure 13. Figure 13(a) shows an ARAMIS fringe plot of axial strain in the vicinity of the center string (S-4). Exterior axial strain gage locations in the same region are indicated on the figure. The results along cross section A-A are plotted in Figure 13(b), showing good agreement between ARAMIS (black line), strain gage results (red squares), and finite element predictions, (unfilled circles).

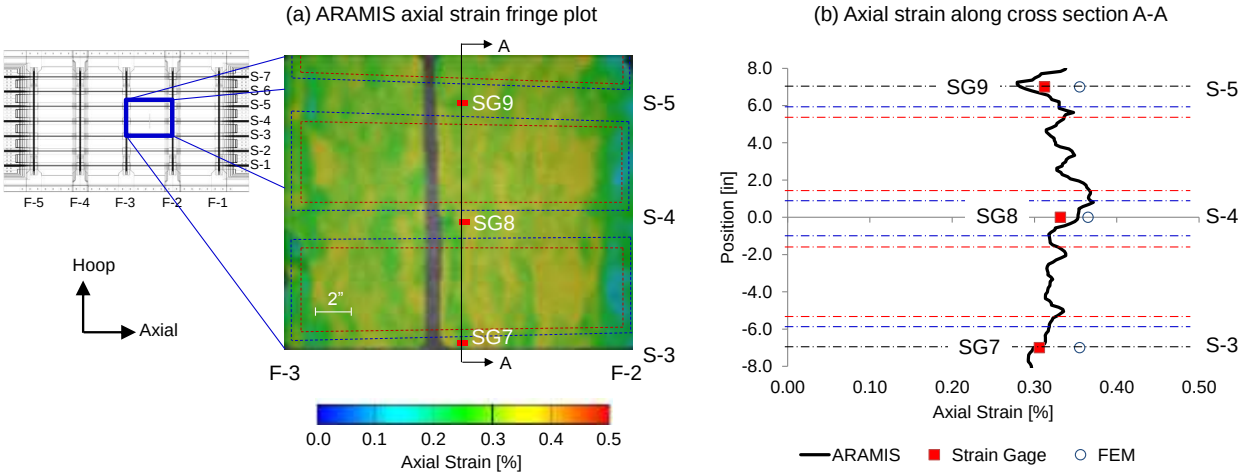

Figure 13. ARAMIS and Strain Gage Results for Combined Limit Load (shown at maximum load)

5.2 Phase II

Phase II included a baseline inspection, an impact, a postimpact inspection, and then application of six load conditions, each of which was followed by inspection. Load conditions for Phase II are defined in Table 1.

5.2.1 Pre- and Postimpact Inspections

The panel was inspected before and after impact using C-Scan and flash thermography. An overview of the results is discussed in the following sections.

5.2.1.1 C-Scan

The C-Scan was performed in the region around the impact location. Figure 14(a) and (c) show the preimpact C-Scan, and Figure 14(b) and (d) show the postimpact C-Scan. The C-Scans are shown at two depths: the depth of the skin and the depth of the flange. The location of the BVID and the delamination that resulted from the impact are identified in Figure 14(b) and (d). Note that between the edge of the stringer flange and the first stitch row, the delamination is significantly longer than the part of the delamination contained between the first and second stitch rows (first and second are relative to the stringer flange edge). Also note that the delamination is completely arrested by the second stitch row. C-Scans were performed after each load condition was applied during Phase II, and no growth of the delamination associated with the BVID was observed, which indicated that the stitch rows arrested any further delamination growth throughout the loading sequences of Phase II.

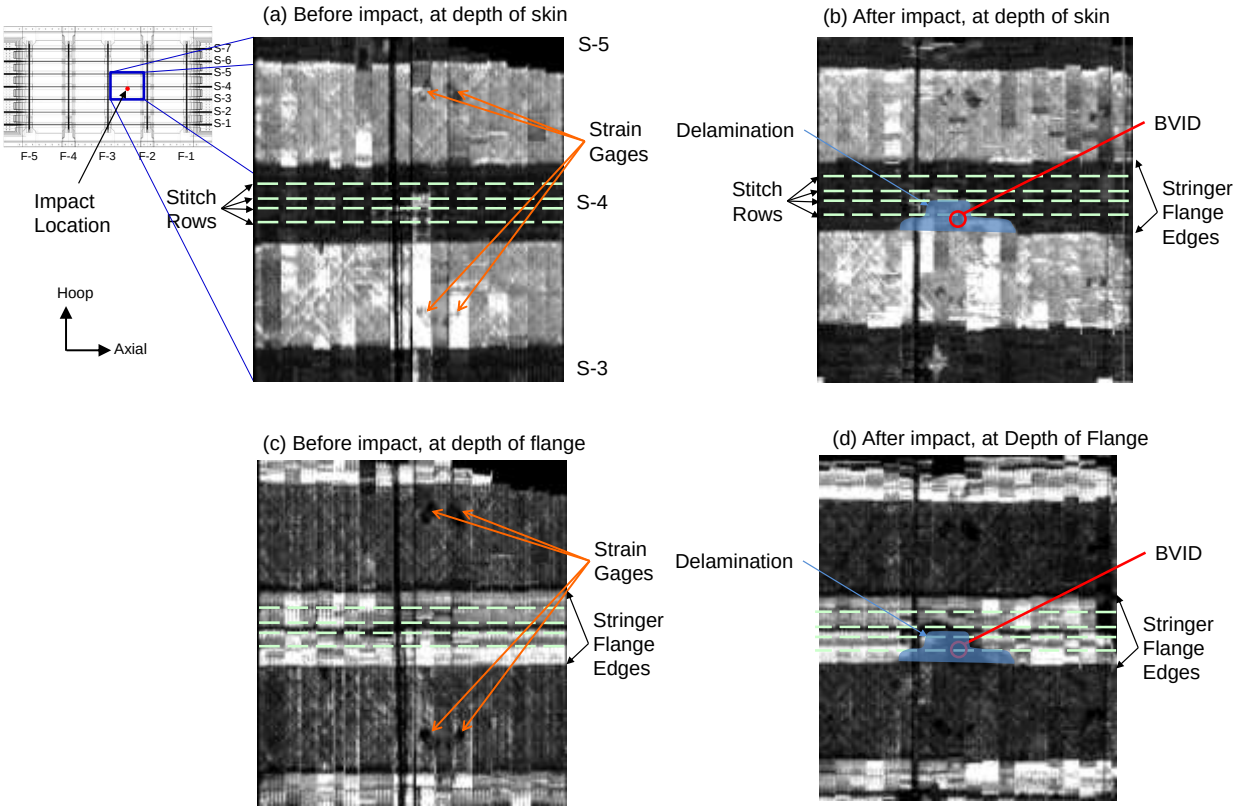

Figure 14. C-Scan for Impact Region

5.2.1.2 Flash Thermography

The flash thermography system was able to identify the damage resulting from the impact, showing a delamination size similar to that found using the C-Scan, as shown in Figure 15. The

presence of the lighter regions immediately to the left and right of the dark circular damage indicate delamination between the stringer flange and skin, highlighted in blue.

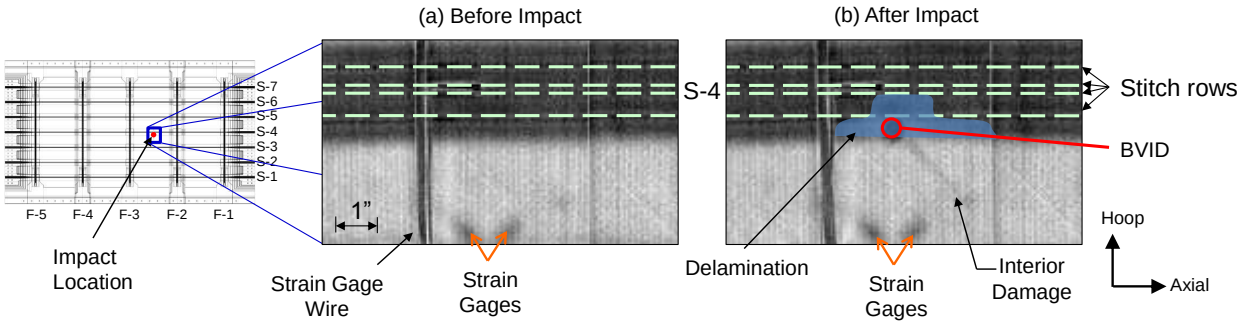

Figure 15. Flash Thermography Results Showing the Second Derivative (2D) of t-T at 2.0 Seconds for the Impact Region

5.2.2 Strain and Displacement

Global strains and displacements at limit load were observed to be nearly identical before and after the impact. Figure 16 shows representative results comparing test section skin strains and axial end displacements between Phase I and II for combined limit load (1P + 100% DLL). These consistent strains indicated no load redistribution due to damage growth.

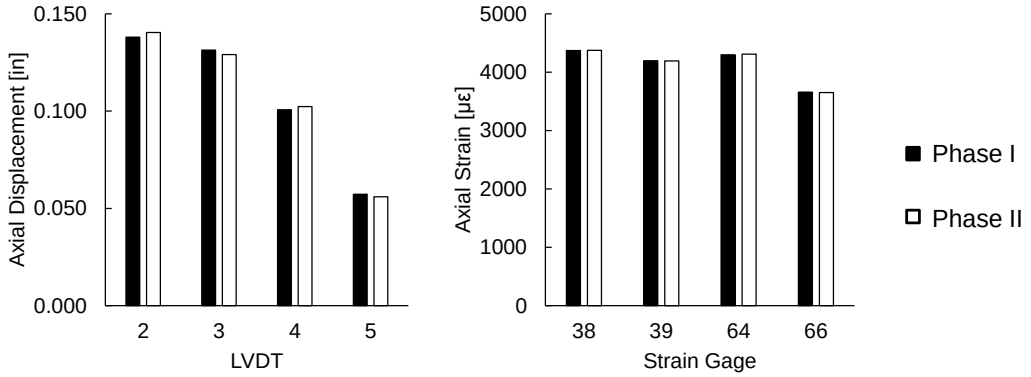

Figure 16. Comparison of Displacements and Strains Before and After Impact for the Combined Load Case

A significant local strain concentration was detected using the ARAMIS system. The axial strain in the vicinity of the BVID and along cross section A-A, is shown in Figure 17 for 150% DLL. The maximum magnitude of axial strain in the vicinity of the BVID remained well below the anticipated material failure strain of 0.9% for the skin [4], which is consistent with the visual observations of no damage growth.

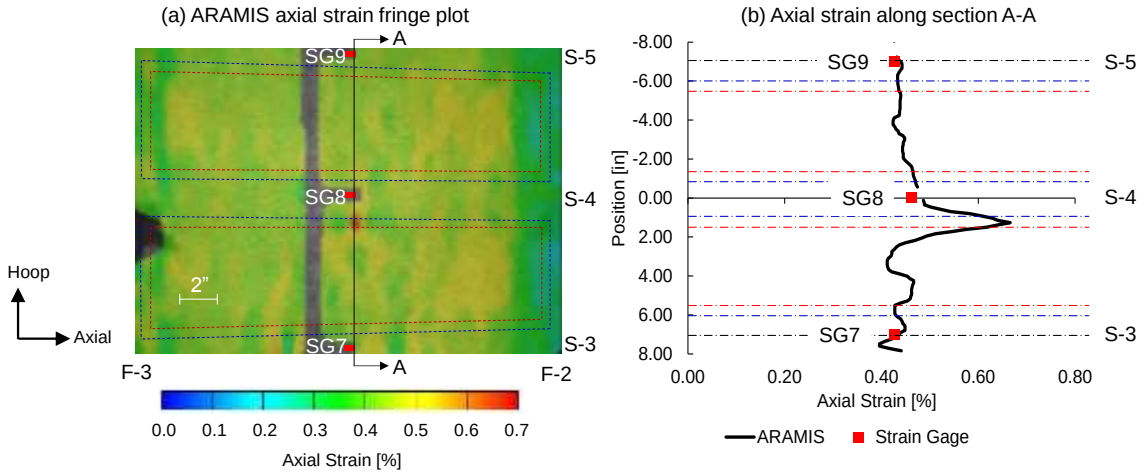

Figure 17. The ARAMIS and Strain Gage Results for Postimpact Loading at 150% DLL, Tension Only

5.2.3 Post Load Inspection

After completion of the Phase II loading, interior and exterior visual, C-Scan, and flash thermography inspections all showed no evidence of BVID growth. Therefore, the stitch rows contained the delamination and did not permit delamination growth up to ultimate load conditions.

5.3 Phase III

A two-bay notch was machined into the panel severing the skin, flange, and central stringer as described previously. A series of five load conditions were applied during Phase III: (1) a pressure loading up to 1.15P was applied, which is the pressure magnitude requirement specified in 14 CFR 25.571, (2) the pressure was reduced to 1P and axial load was applied up to 100% DLL, (3) the pressure load was removed while the 100% DLL axial load was maintained, (4) pressure was increased back to 1P, and (5) axial load was increased, while keeping the pressure constant, until the panel exhibited catastrophic failure. This sequence is shown in Figure 18 where the orange line indicates the pressure and the blue line indicates the axial load. The key observations made throughout the load history of the final load sequence are also summarized in Figure 18, including the period in which damage was contained to a two-bay region (blue bar), and the periods of damage formation (red bars).

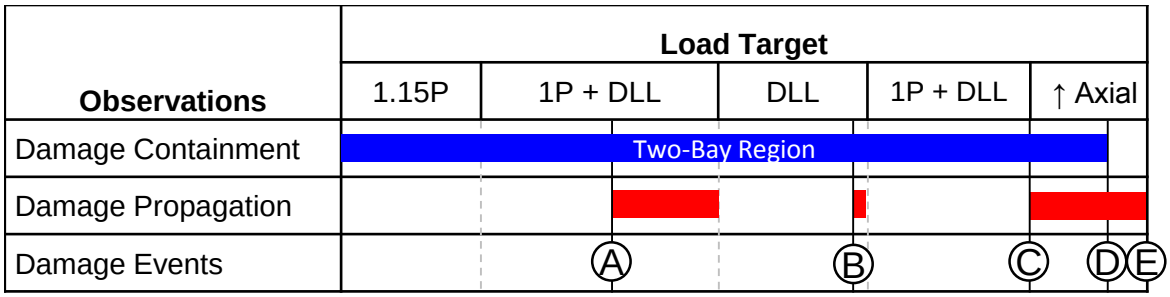

Figure 18. Load Case III-F Timeline Summarizing Damage Containment, Damage Propagation, and Damage Events (A-E)

Starting during load step 2 and continuing until catastrophic failure, damage was observed visually and was evidenced through strain redistribution at several instances throughout the loading sequence. The key damage events are lettered A-E in Figure 18 and are summarized in Table 3.

Table 3. Key Damage Events

Damage Event	Load	Visual Observations
A	1P + 58% DLL	Damage formation. Propagates until load step two.
B	100% DLL	Single damage formation event on interior surface.
C	1P + 100% DLL	Damage propagation. Continues until load step five.
D	1P + 160% DLL	Damage propagates beyond the two-bay region.
E	1P + 184% DLL	Catastrophic failure.

5.3.1 Load Step 1: Pressure Load (1.15P)

In load step 1, pressure was increased to 1.15P. No damage was detected during this loading, consistent with the analytical predictions. Unfortunately, water used to pressurize the panel leaked through the sealed notch region, which disrupted ARAMIS data collection. The panel surface was dried prior to the next load step so that ARAMIS data collection could continue.

5.3.2 Load Step 2: Combined Load (1P + 100% DLL)

In load step 2, a combined load of 1P + 100% DLL was applied. Visible damage formation was first observed at a combined load of 1P + 58% DLL in the form of a matrix crack on the internal surface that propagated from the notch tips symmetrically. This damage initiation is shown as damage event A. Shortly after, at a combined load of 1P + 70% DLL, damage was observed visually on the external surface in the same mode. There was no drop in load carrying capability due to this damage.

Prior to the external surface damage formation, ARAMIS and strain gage results showed excellent correlation to each other. Axial strain fringe patterns computed using ARAMIS showed the characteristic kidney-shaped strain concentration at the notch tip, as shown in Figure 19(a). The correlation between ARAMIS and strain gage 7 immediately prior to the damage formation at notch tip A is shown in Figure 19(b), and the load history prior to damage formation is shown in Figure 19(c). The black line in the figure represents ARAMIS axial strain, and the red square and line indicate the axial strain measured by strain gage 7. The two large spikes in the ARAMIS strain history data near the 1.15P load condition are artifacts in the data from the water leakage.

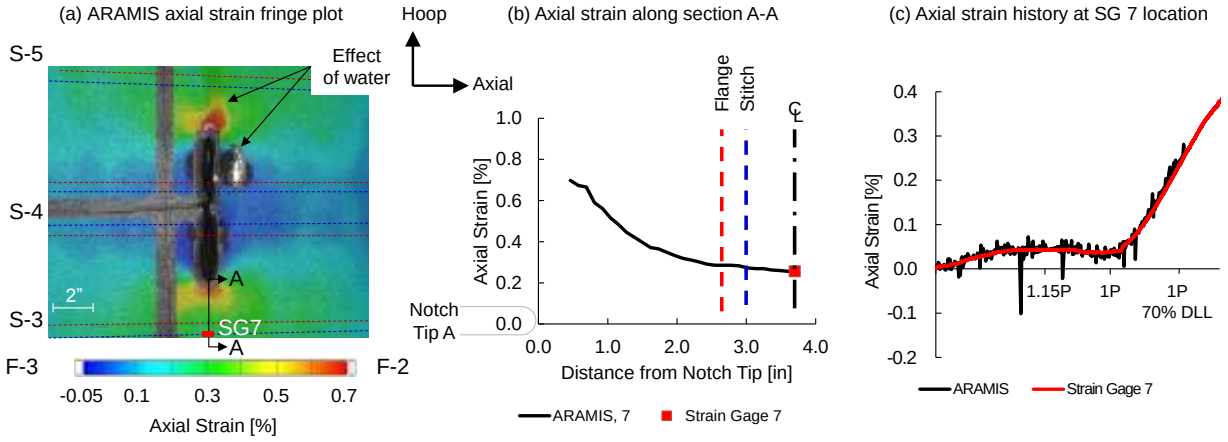

Figure 19. Axial Strain at 1P + 70% DLL Showing Excellent Agreement Between ARAMIS and Strain Gage Results

Normal strains along 0-, 45-, and 90-degree sections from notch tip A at the same load level (shown in Figure 20) indicate that notch tip strains are approaching the material failure strain, which is in agreement with the observed visual damage initiation at this load level.

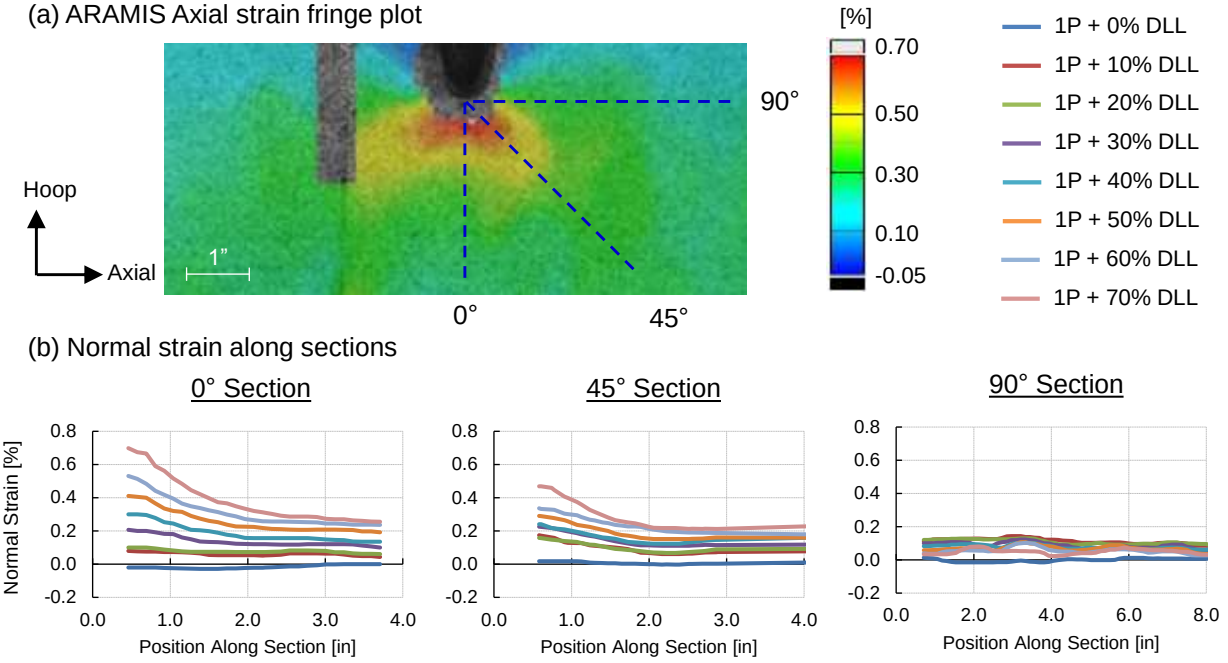

Figure 20. The ARAMIS Axial Strain Distribution at the Notch Tip for 1P + 70% DLL and Section Plots Showing Normal Strain Along 0°, 45°, and 90° Sections.

As axial load increased and damage propagated, significant water leakage occurred, thus disrupting the ARAMIS data recorded after the initiation of local failure.

Figure 21 shows photographs of the damage propagation sequence on the exterior surface during load step two. The gray area progressing out from the notch tip is the water leakage path. Figure 21(b) shows visible damage formation measuring about 0.1 inch at a combined load of 1P + 70% DLL.

Throughout the remainder of load step two (beyond damage event A), exterior damage propagation continued in the 45° orientation, parallel to the surface ply fiber direction, indicating a matrix cracking damage mode. Figure 21(c) shows an intermediate load level where damage is clearly visible and measures 0.5 inch. Figure 21(d) shows the extent of damage at the end of load step two, where the visible crack had propagated 1.3 inch from the notch tip.

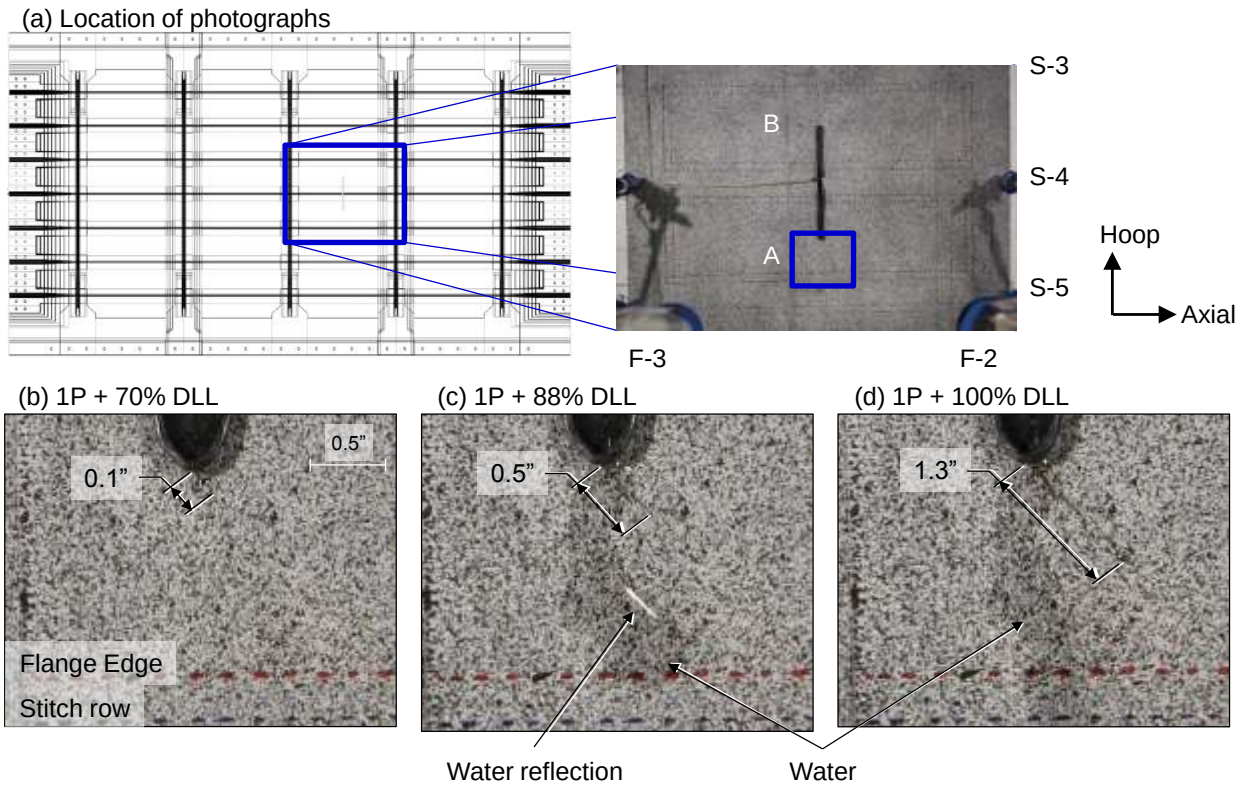

Figure 21. Photographs of Damage Propagation From Damage Event A During Load Step 2, Showing the External Surface of Notch Tip A

Visual observations of the interior of the panel showed more damage accumulation than on the external surface. Visible damage on the interior skin was also 45° matrix cracking, similar to damage observed on the exterior skin. Shortly after damage formation, three of the four interior-skin notch tip strain gages (45, 48, and 49) failed, indicating that damage reached the gage. There was no drop in load carrying capability due to damage formation and propagation load step two.

5.3.3 Load Step 3: Axial Load (100% DLL)

In load step 3, the pressure load was reduced to zero while maintaining 100% DLL. During load step 3, damage propagation was observed on the interior surface only, denoted as damage event B. Figure 22 shows before and after photographs of the damage event, where damage propagates to the adjacent stringer flange.

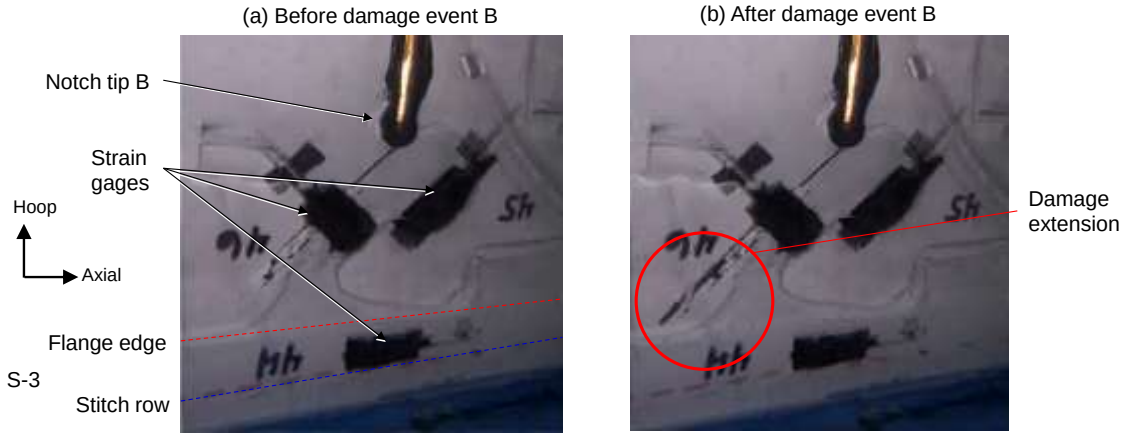

Figure 22. Photographs of the Interior Surface Showing Damage Propagation From Notch Tip B

5.3.4 Load Step 4: Combined Load (1P + 100% DLL)

In load step 4, pressure was increased up to loading of 1P + 100% DLL. As expected, no damage propagation was observed during this load step because the panel had been loaded to this level in load step 2.

5.3.5 Load Step 5: Catastrophic Failure Load (1P + Increasing Axial Load)

In load step 5, pressure was held constant at 1P, while axial load was increased until catastrophic failure occurred. As the axial load was increased above DLL, visually observed damage propagation continued, indicated as damage event C.

5.3.5.1 Exterior Surface Visual Damage Propagation Observations

Photographs of the damage propagation on the exterior surface from damage event C to D (axial load increased from 100% to 160% DLL) at notch tip A are shown in Figure 23, with the same orientation and scale as Figure 21.

Visual damage propagation was slow, stable, and in a 45° orientation from the notch tip up to 1P + 134% DLL and was arrested by the inner row of stitching, as shown in Figure 23(a) through (f). As the load reached 1P + 140% DLL, damage at notch tip A propagated instantaneously from the stringer flange, to the center stitch row and was once again arrested, as shown in Figure 23(f) and (g), respectively. Additional axial load was required to propagate the damage beyond the stringer. The load reached 1P + 160% DLL, as shown in Figure 23(h), at which point damage propagated instantaneously beyond the two-bay region (damage event D) and out of the exterior surface field of view, as shown in Figure 23(i). This damage propagation created a 5% axial load drop, indicating a reduction in the stiffness of the panel.

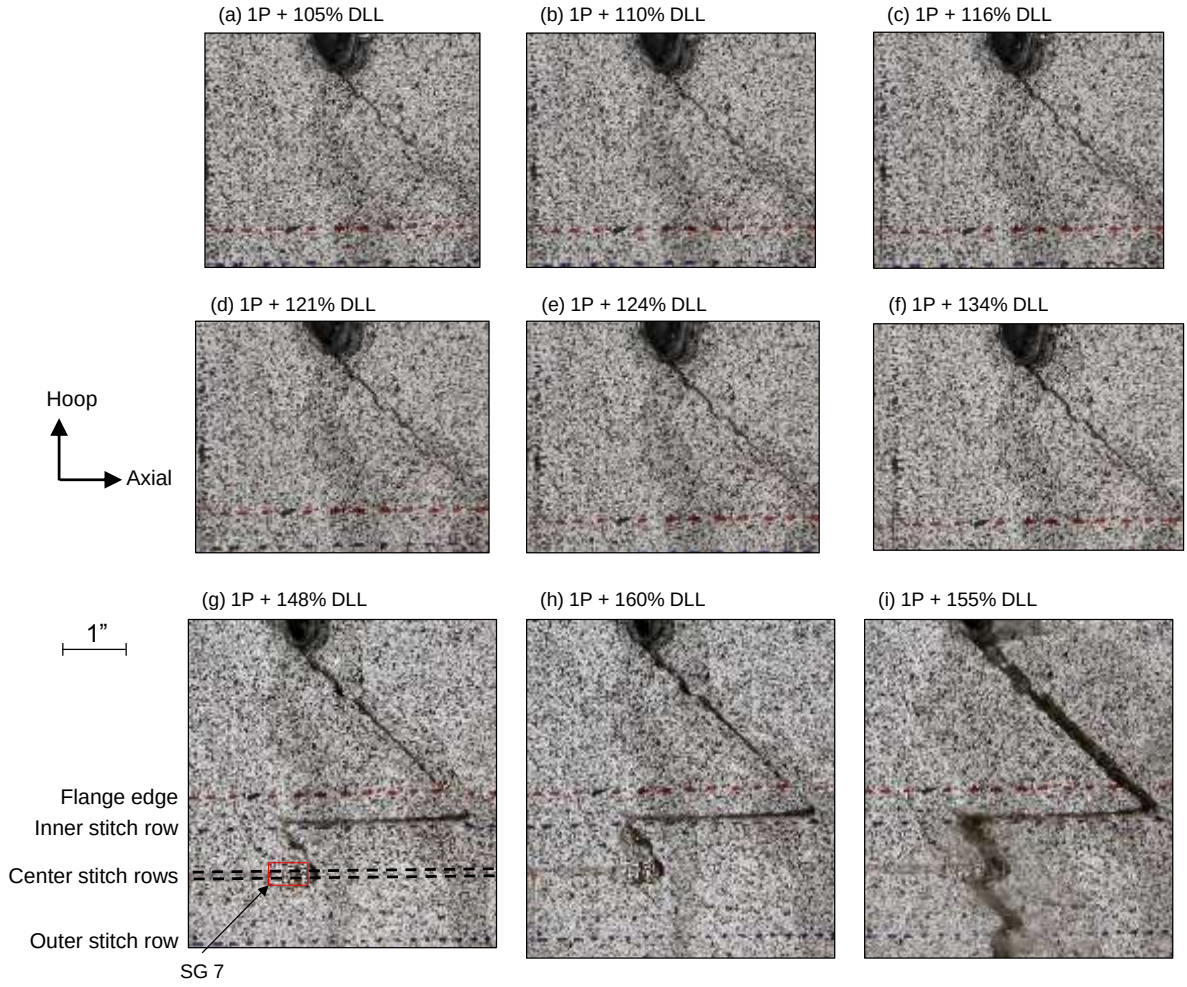

Figure 23. Exterior Surface Damage Propagation From Damage Event C to D at Notch Tip A

The high-speed camera was used to capture damage event D at the opposite notch tip (notch tip B), where damage propagated beyond the two-bay region. The damage propagation was analogous to the notch tip A results shown in Figure 23(h) and (i), however the damage behaved slightly differently. The damage had been arrested by the inner stitch row up to 1P + 160% DLL and then propagated past the other stitch rows nearly instantaneously. The four high-speed camera frames that captured this event, which are 0.2 milliseconds apart, are shown in Figure 24. The images are marked with a red dot to indicate the extent of visual damage propagation observed in images (a) through (c). In image (d), the red dot indicates that damage extended at least to the edge of the field of view. The damage was briefly arrested (duration was approximately 0.4 ms) at the outer stitch row, as shown in Figure 24(b) and (c).

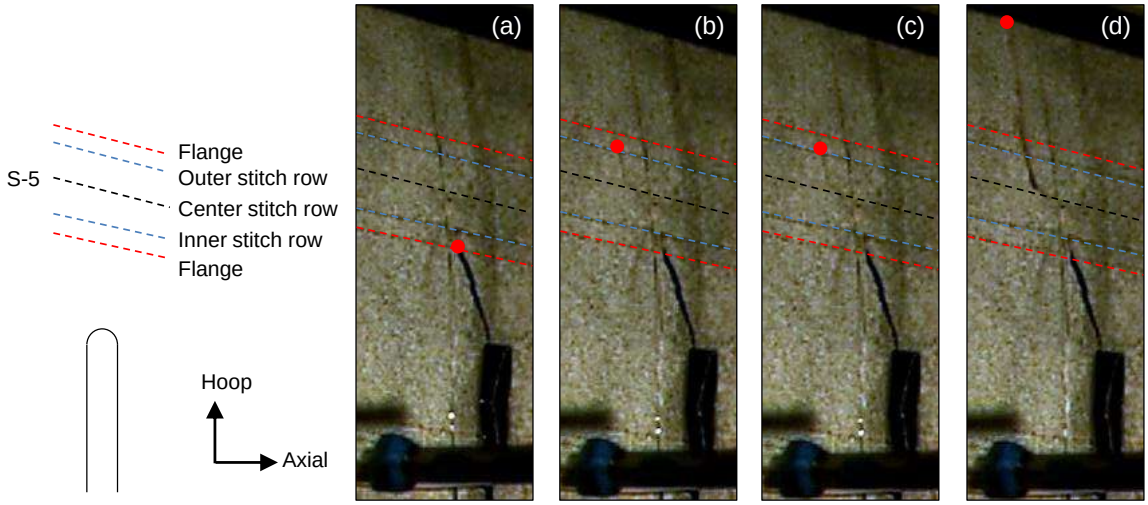

Figure 24. Sequential Frames Captured Using a High-Speed Camera Showing Damage Propagation Beyond the Two-Bay Region

5.3.5.2 Interior Surface Visual Damage Propagation Observations

Damage visible on the interior surface was much more widespread than on the exterior surface. As the load was increased from damage event C, visual observations on the interior surface showed slow, stable damage accumulation ahead of both notch tips, which propagated to the adjacent stringer flange edges, as shown schematically in Figure 25(a) and (b). At 1P + 140% DLL, cracks formed instantaneously along both adjacent stringer flanges indicating a delamination between the free edge of the stringer and the skin, as shown in Figure 25(c). The interior damage was subsequently arrested by the stitching in the frame flanges as load was increased leading up to damage event D. Prior to damage event D, all the damage had been completely contained within the two-bay region by the stitching through the flanges of the surrounding stiffeners.

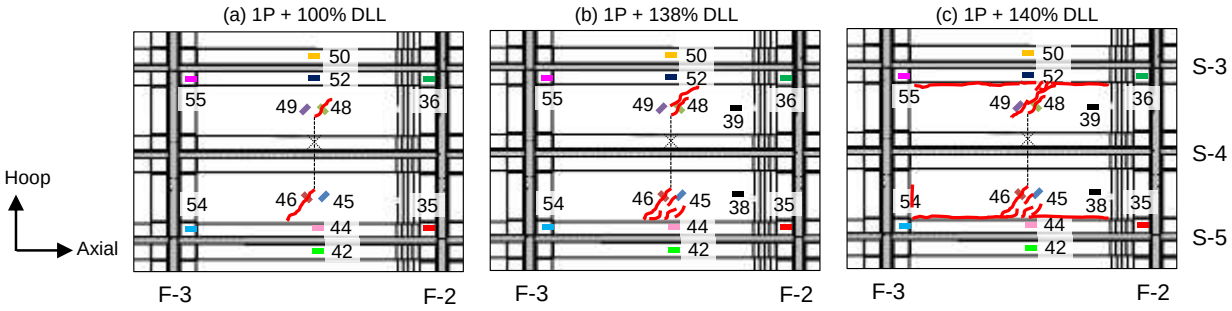

Figure 25. Observed Visual Damage Accumulation on the Interior Surface (a) After Damage Event B and (b) Before and (c) After Delamination Formation

5.3.5.3 Strain Redistributions

Damage propagation was also evident through several strain redistributions as axial load was increased beyond damage event C, as shown in Figure 26. Detailed strain gage locations are

shown in Figure 26(a) and (b). The overall axial displacement is shown in Figure 26(c), and strain measurements are shown in Figure 26(d) through (h).

The first evidence of strain redistribution occurred at 1P + 140% DLL as damage propagated instantaneously to the adjacent stringer's center stitch row (refer to Figure 23(f) and (g)). This strain redistribution was observed in the exterior skin strain gages above the adjacent stringers (SG 7 and 9), as shown in Figure 26(d). Strain gage 7 showed a particularly large discontinuity as damage propagated directly next to the gage (see Figure 23(g)). A small strain reduction discontinuity in the interior skin gages (SG 38 and 39) in the two-bay region, as shown in Figure 26(e), and in the stringer flange gages (SG 44 and 52) in the two-bay region, as shown in Figure 26(g), indicated load carried by the skin was slightly reduced due to the damage event. This small strain redistribution had very little effect on the overall load carrying capability.

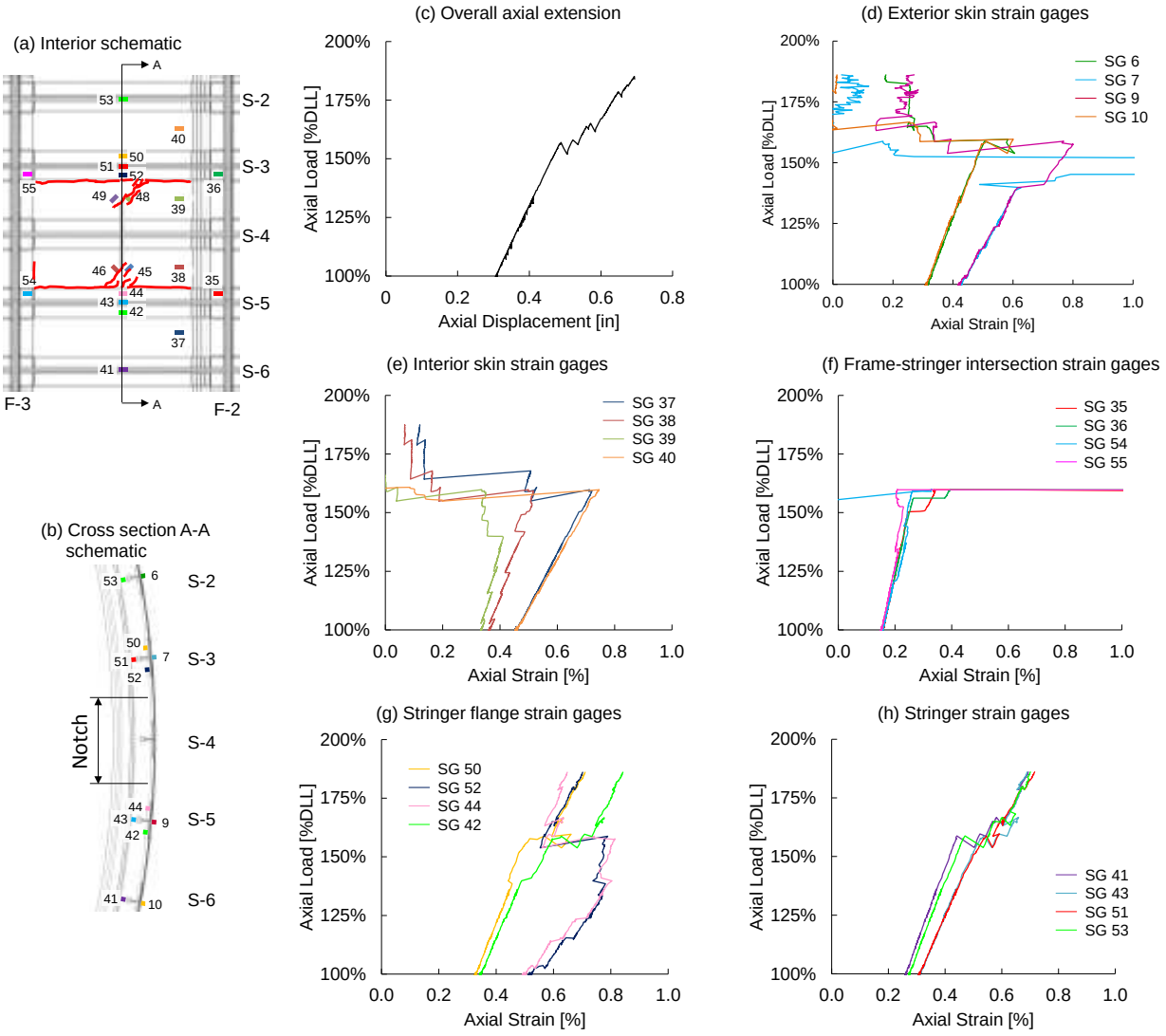

Figure 26. Selected Strain and Displacement Results and Locations Between Load Steps 4 and 5

Shortly after, as the load was increased beyond 1P + 140% DLL, the damage propagated parallel to the adjacent stringers delaminating the unstitched edged of the stringer flanges to the stringer frame intersections and was arrested by the stitching in the frame flanges. This damage growth is evidenced by the strain discontinuities of the strain gages located at the frame and stringer intersections, (SG 35, 36, 54, and 55) shown in Figure 26(f) near 1P + 150% DLL applied load.

At damage event D (1P + 160% DLL), several strain discontinuities occurred, indicating significant load redistribution from the skin to the stringers. Strain on the internal surface of the skin in the vicinity of the damage (SG 38 and 39) dropped to near zero, indicating the failure of the skin in this region. Strains on the stringer flanges closest to the notch (SG 44 and 52) reduced by 0.25%, while strains on the stringer's other flanges (SG 42 and 54) increased, indicating load transfer to the stringers and suggesting failure of the first stitch row as damage delaminated the stringer flange from the skin. A discontinuity in axial displacement also occurred, as shown in Figure 26(c).

Limited interior and no exterior visual observations where made of the damage propagation from damage events D to E because the field of view was limited by the loading fixture, which obstructed portions of the panel. It is likely that the damage was contained within the four-bay region contained by stringers S-2 and S-6 until 1P + 167% DLL, at which point damage propagated to the outermost stringers. At this load level, note that the strains in stringers S-2, S-3, S-5, and S-6 (as measured by SG 41, 43, 51, and 53, respectively) become uniform, as shown in Figure 26(h). At the same time, skin strains are very low, as shown in Figure 26(d) and (e), indicating the stringers are bridging the failed skin and carrying the load. It is also observed that the skin in the bay between stringers S-5 and S-6 maintained higher strains than the corresponding bay between stringers S-2 and S-3, which indicates that the failure was not symmetric. These skin strains suggest that, at this time, the damage was more severe in the bay between stringers S-5 and S-6 than in the bay between stringers S-2 and S-3.

At catastrophic failure, damage event E, the skin was almost entirely failed, as shown by the low strains in the skin strain gages. The final failure occurred when several stringers were pulled-out of the load introduction area at 1P + 184% DLL.

5.3.6 Postfailure Inspection

Postfailure inspection was used to identify failure mechanisms. Visual and thermography inspections were conducted. Visually damage was observed to be more widespread on the interior than the exterior. The damage followed a tortuous path, which was not self-similar or symmetrical. Figure 27 shows a side-by-side comparison of an exterior surface photograph, an interior surface photograph, and flash thermography results. The through-the-thickness damage was contained within frame F-2 and F-3. The damage path was altered at several of the locations where it crossed the stitching rows, demonstrating the ability of the stitch rows to turn and contain damage.

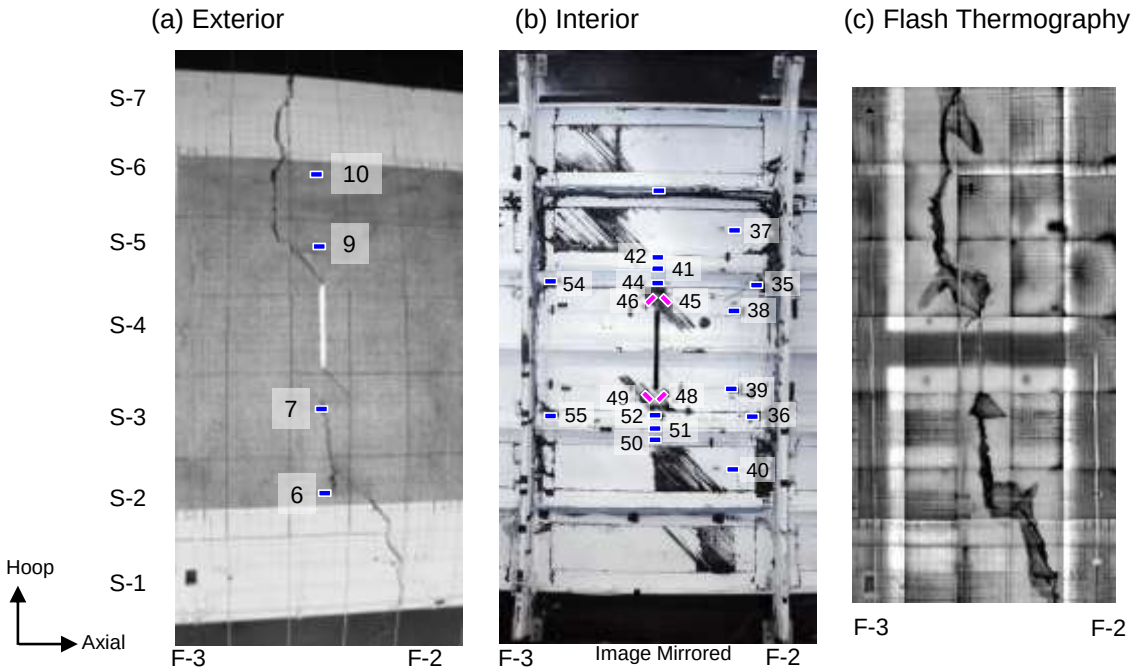

Figure 27. Postfailure (a) Exterior Surface Photo, (b) Internal Surface Photo (mirrored for direct comparison), and (c) Flash Thermography Results (1D, t = 5s)

Visual inspection showed stitch and stringer failures. Stitch failures were widespread, resulting in delamination of the frame and stringer flanges from the skin. A majority of the stitch failure occurred during the sudden release of energy at catastrophic failure.

Stringer rod, web, and flange pullout occurred in three of the stringers, S-3, S-5, and S-6, as shown in Figure 28. Visual evidence suggests that the stringer wrap plies, webs, and flanges delaminated from the surrounding load introduction buildup and skin plies. Failure at the stringer and frame intersections (keyhole), circled in red in Figure 28, indicates that the stringers displaced axially, relative to the frame.

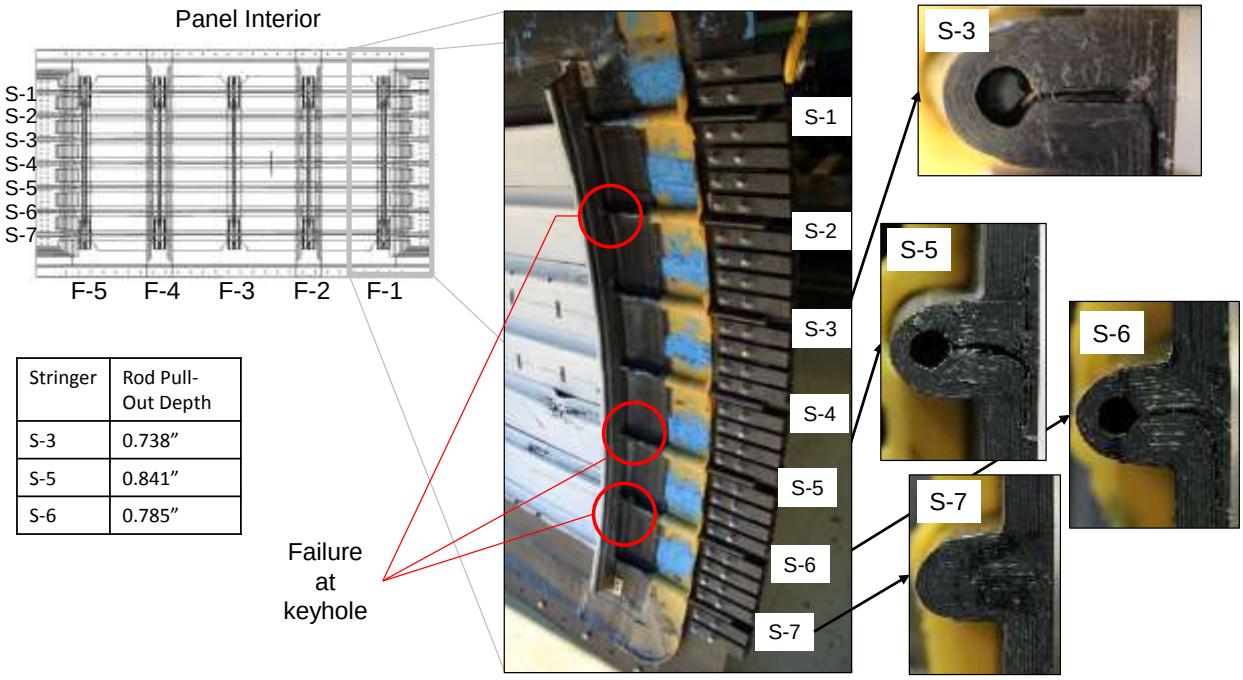

Figure 28. Evidence of Stringer Rod, Web, and Flange Pullout in Stringers S-3, S-5, and S-6

The Phase III results showed that the stitched panel contained the damage within the two-bay region up to 1P + 160% DLL. Catastrophic failure occurred in the load introduction region at 1P + 184% DLL, which was well above the test criterion of 1P + 100% DLL.

VI. SUMMARY

In summary, the purpose of this joint test program was to show that a curved PRSEUS panel meets the strength, deformation, and damage tolerance requirements of Title 14 CFR Part 25, and to characterize the damage containment features of a curved PRSEUS panel. For this purpose a curved PRSEUS panel was tested in axial tension, internal pressure, and combined axial tension and internal pressure in a pristine condition, with BVID, and with a two-bay notch that severed the central stringer and adjacent skin. All tests were conducted at the FAA FASTER facility. Pristine condition test results provided a baseline by testing the panel in the as-built condition. The results showed linear strain and displacement results in all pristine condition load cases. BVID was introduced into the panel through drop weight impacts, resulting in nonpenetrating visual damage including matrix cracking, fiber breaks, and delamination between the skin and stringer flange. After ultimate load conditions were applied, visual and other nondestructive inspections showed no damage growth, which exceeds the design goal of no damage growth at limit load. Finally, a two-bay notch was machined, severing the central stiffener and adjoining skin. The panel was then subjected to limit-load conditions, followed by combined 1P (9.2-psi) pressure while increasing axial tension load to catastrophic failure. Damage was contained within the two-bay region by the stitching rows up to 1P + 160% DLL. Axial load was further increased until catastrophic failure, when several stringers pulled out from the load introduction area at 1P + 184% DLL, well above the design goal of catastrophic failure just above limit load. The three phases of testing showed compliance with select requirements

from Title 14 CFR Part 25; of course, future testing of several damage conditions including environmental effects is necessary satisfy all requirements. These test results further verify the damage containment features of the PRSEUS concept and suggest its appropriateness for future flight vehicles.

VII. ACKNOWLEDGEMENTS

The authors would like to acknowledge Yongzhe Tian, Jeff Panco, and Patrick Sheehan whose diligent efforts during the FASTER modifications and testing played an instrumental role in this team effort. The authors would also like to acknowledge the support of Patrick Johnston who performed the numerous ultrasonic examinations of the panel.

VIII. REFERENCES

[1] Jegley, D., Velicki, A., and Hansen, D., "Structural Efficiency of Stitched Rod-Stiffened Composite Panels With Stiffener Crippling," *49th AIAA/ASME/ASCE/AHS/ASC Structures, Structural Dynamics and Materials Conference*, Schaumburg, IL, April 7-10, 2008.

[2] Velicki, A., "Advanced Structural Concept Development Using Stitched Composites," *49th AIAA/ASME/ASCE/AHS/ASC Structures, Structural Dynamics and Materials Conference*, Schaumburg, IL, April 7-10, 2008.

[3] Li, V. and Velicki, A., "Advanced PRSEUS Structural Concept Design and Optimization," *12th AIAA/ISSMO Multidisciplinary Analysis and Optimization Conference*, AIAA-2008-5840, Victoria, British Columbia, Canada, September 10-12, 2008.

[4] Velicki, A., "Damage Arresting Composites for Shaped Vehicles," NASA/CR-2009-215932, 2009.

[5] Air Vehicle Technology Integration Program (AVTIP), Delivery Order 0059: Multi-role Bomber Structural Analysis, AFRL-VA-WP-TR-2006-3067, Krishna Hoffman, May 2006, Final Report for December 14, 2004 - May 8, 2006.

[6] "Airworthiness Standards: Transport Category Airplanes," Title 14 Code of Federal Regulations, 2011.

[7] Bergan, A., Bakuckas, J., Lovejoy, A., Jegley, D., Linton, K., Korkosz, G., Awerbuch, J., and Tan, T.M., "Full-Scale Test and Analysis of a PRSEUS Fuselage Panel to Assess Damage-Containment Features," *2011 Airworthiness and Sustainment Conference*, San Diego, CA, April 18-21, 2011.

[8] Federal Aviation Administration, Advisory Circular (AC 20-107B), "Composite Aircraft Structure," August 8, 2009.

[9] Federal Aviation Administration, Advisory Circular (AC 25.571-1D), "Damage Tolerance and Fatigue Evaluation of Structure," January 13, 2011.

[10] Linton, K., Neal, A., Mills, G., Velicki, A., and Thrash, P., "Design, Analysis, and Fabrication of a Curved PRSEUS Panel," Final report for NASA contract: NNL04AA11B/task order: NNL10AA99T, December, 2010.

[11] ARAMIS User Manual—Software (ARAMIS v6.1 and higher), GOM GmbH., August 2009.